AGU PUBLICATIONS

JGR

Journal of Geophysical Research: Oceans

RESEARCH ARTICLE

10.1002/2013JC009469

**Key Points:**
- Even below a turning depth tidal flow over topography generates internal tides
- Linear theory with an effective stratification predicts internal tide power
- Internal tides generated below a turning depth are insensitive to topographic shape

**Correspondence to:**
M. S. Paoletti,
mpaoletti@chaos.utexas.edu

**Citation:**
Paoletti, M. S., M. Drake, and H. L. Swinney (2014), Internal tide generation in nonuniformly stratified deep oceans, *J. Geophys. Res. Oceans*, *119*, 1943–1956, doi:10.1002/2013JC009469.

Received 28 SEP 2013
Accepted 20 FEB 2014
Accepted article online 27 FEB 2014
Published online 17 MAR 2014

# Internal tide generation in nonuniformly stratified deep oceans

**M. S. Paoletti[1], Matthew Drake[1], and Harry L. Swinney[1]**

[1]Department of Physics, Center for Nonlinear Dynamics, University of Texas at Austin, Austin, Texas, USA

**Abstract** We present numerical and experimental studies of the conversion of tidal motions of an exponentially stratified fluid over two-dimensional knife edge, Gaussian, and complex bottom topography to radiated internal waves in a model of the deep ocean. We compare the radiated internal wave power for cases of strong stratification, where the buoyancy frequency profile $N(z)$ (proportional to the square root of the density gradient) is much larger than the tidal frequency $\omega$, to the power radiated for weak stratifications. We consider particularly internal wave generation for topography below a turning depth $z_{\mathrm{td}}$, where $N(z_{\mathrm{td}})=\omega$; for $z < z_{td}$, internal waves are evanescent. We find that topography below a turning depth does generate internal waves that propagate for $z > z_{td}$, although the radiated power in these waves is much weaker than in cases without turning depths. The radiated power is predicted well by prior analytical theory if the nonuniform stratification is averaged over depths spanning from the bottom boundary up to an effective height $z_{\mathrm{eff}}$. In the absence of a turning depth, we find $z_{\mathrm{eff}}$ is approximately equal to the height of the topography, indicating that only the stratification for depths spanned by the topography is relevant. However, in the presence of a turning depth, the vertical scale of the internal tide becomes larger, and $z_{\mathrm{eff}}$ increases approximately linearly with the turning depth height toward values comparable to the total fluid depth.

## 1. Introduction

Internal waves produce a significant fraction of the mixing required to maintain the thermohaline circulation in the oceans [*Munk and Wunsch*, 1998]. The energy spectrum of internal waves in the oceans is dominated by the semidiurnal lunar tidal frequency $\omega_{M2}=1.4052\times10^{-4}\mathrm{rad/s}$ and near-inertial frequencies, as tidal and rotational motions over bottom topography are efficiently converted into propagating internal waves. Approximately half of the internal wave energy in the ocean [*Wunsch and Ferrari*, 2004] is produced by tidal interactions with continental slopes [*Cacchione et al*., 2002; *Moum et al*., 2002; *Nash et al*., 2004], seamounts [*Lueck and Mudge*, 1997; *Kunze and Toole*, 1997], ridges [*Rudnick et al*., 2003; *Klymak et al*., 2006], and rough topography in the deep ocean [*Polzin et al*., 1997; *St Laurent et al*., 2001], producing internal waves, known as internal tides. The impact of internal tides on the global ocean energy budget depends on the power converted from tidal motions into radiated internal waves. In order to determine the impact of internal waves on the global ocean energy budget, it is useful to determine the power converted from tidal motions into radiated internal waves

$$P_{\mathrm{IW}}=\int\int \mathbf{\Phi}\cdot\hat{\mathbf{n}}\,dS, \tag{1}$$

where $\mathbf{\Phi}=\langle p'\mathbf{v}'\rangle$ is the baroclinic energy flux, $p'$ is the perturbed pressure, $\mathbf{v}'$ is the perturbed velocity, brackets $\langle\rangle$ indicate temporal averages over an integer number of tidal periods, and $\hat{\mathbf{n}}$ is a unit vector normal to a surface $S$ that contains the topographic feature of interest.

To characterize the efficiency of the conversion of tidal motions over topography to internal waves, we compare the radiated internal wave power $P_{\mathrm{IW}}$ to an estimate of the tidal power that interacts with the topography

$$P_{\mathrm{tide}}=HL_y\Phi_{\mathrm{tide}}, \tag{2}$$

where $H$ is the topographic height, $L_y$ is the length of the topography in the direction orthogonal to the tidal flow and gravity, and $\Phi_{\mathrm{tide}}$ is the maximum tidal energy flux. We estimate the tidal energy flux for a tidal flow, given by $\boldsymbol{u}_{\mathrm{tide}}=\hat{\boldsymbol{x}}A\omega\cos\omega t$, to be

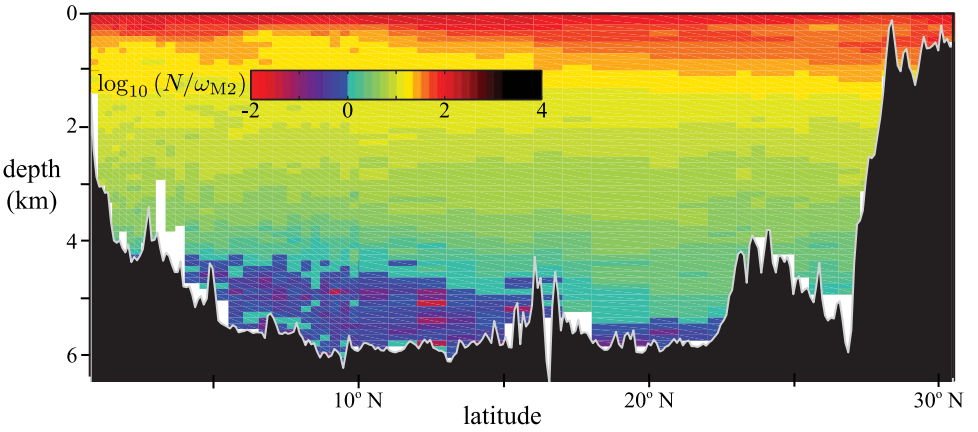


**Figure 1.** The local buoyancy frequency $N$ decreases by more than two orders of magnitude with depth and in the abyss becomes less than the semidiurnal lunar tidal frequency $\omega_{M2}$ at some locations. Internal tides become evanescent beneath turning depths where $N = \omega_{M2}$, indicated by the abrupt change in color from green to dark blue (cf. logarithmic color bar). The buoyancy frequencies are computed using data from the *World Ocean Circulation Experiment* [1994] transect P08, which followed a meridional path from Indonesia to Japan (figure adapted from *King et al*. [2012]).

$$\mathbf{\Phi}_{\text{tide}} = \hat{\mathrm{x}}\rho_0 A^2\omega^3 H, \tag{3}$$

where the pressure scale is set by $\rho_0 A\omega^2 H$, the velocity scale is given by $A\omega$, $A$ is the tidal excursion, $\omega$ is the tidal frequency, and $\rho_0$ is a reference density. We characterize the conversion of tidal motions to internal waves through the normalized power

$$\tilde{P} = \frac{P_{\text{IW}}}{P_{\text{tide}}} = \frac{P_{\text{IW}}}{\rho_0 H^2 A^2 \omega^3 L_y}. \tag{4}$$

We conduct laboratory experiments and numerical simulations of the Navier-Stokes equations for tidal flow of a two-dimensional stratified fluid flow over knife edge, Gaussian, and complex topography. We consider exponential stratifications with $N(z)$ decreasing with depth, such that $N(z) < \omega$ below a turning depth where $N(z_{\text{td}}) = \omega$; for $z < z_{td}$ the internal waves are evanescent (exponentially damped). Evanescent internal waves have long been studied experimentally [*Mowbray and Rarity*, 1967] and theoretically [*Bell*, 1975a; *Hurley and Keady*, 1997; *Sutherland*, 2010]. Recently, *Kistovich and Chashechkin* [1998] developed a linear theory that describes the propagation of internal waves in arbitrary stratifications, including those that contain a turning depth. *Paoletti and Swinney* [2012] conducted experiments and computations that were found to agree well with the predictions of the Kistovich-Chashechkin theory.

In the ocean, the buoyancy frequency profiles $N(z)$ are typically exponential [see *King et al*., 2012; *Paoletti and Swinney*, 2012, Figure 1a]. *Munk* [1981] suggested the possibility of turning depths for internal waves generated by the $M2$ semidiurnal tide (where $N(z_{\text{td}}) = \omega_{M2}$). The existence of such turning depths was confirmed in a recent analysis of data from the World Ocean Circulation Experiment, as illustrated in Figure 1 for data obtained in a meridional transect in the Pacific, where turning depths exist for latitudes $3-22^{\circ}$N [*King et al*., 2012]. *King et al*. [2012] found that turning depths are common for ocean depths in excess of 4 km (52% of the ocean has depth greater than 4 km), but the generation of internal waves by topography beneath a turning depth has not been considered.

We vary the height of the turning depth by changing the tidal frequency $\omega$ to compare cases without turning depths to those where the turning depth completely envelops the topography. We determine the normalized power $\tilde{P}$ of the internal wave beams for varying turning depth heights $z_{\text{td}}$, topographic widths, and stratifications.

## 2. Prior Work

Past theoretical studies obtained estimates of the internal wave power radiated by tidal flow over isolated, two-dimensional topography [*Baines*, 1973; *Bell*, 1975b; *Llewellyn Smith and Young*, 2002; *Balmforth et al*.,

2002; *Khatiwala*, 2003; *Llewellyn Smith and Young*, 2003; *St Laurent et al*., 2003; *Pétrélis et al*., 2006; *di Lorenzo et al*., 2006; *Garrett and Kunze*, 2007; *Echeverri and Peacock*, 2010; *Zarroug et al*., 2010]. In summary, these studies predict that the radiated internal wave power in a uniformly stratified fluid is given by

$$P_{\text{theory}} = \rho_0 H^2 A^2 \omega^2 \sqrt{N^2 - \omega^2} L_y f(\epsilon), \tag{5}$$

where $N(z) = \sqrt{-(g/\rho_0)(\mathrm{d}\rho/\mathrm{d}z)}$ is the buoyancy frequency, assumed to be constant, and $\epsilon = S_{\text{topo}}/S_{\text{IW}}$ is the criticality parameter, which compares the maximum topographic slope $S_{\text{topo}}$ to the internal wave slope, $S_{\text{IW}} = \omega/\sqrt{N^2 - \omega^2}$ (in the absence of rotation). The function $f(\epsilon) \to \pi/8$ as $\epsilon \to 0$, and smoothly increases to $f(\epsilon) = \pi/4$ as $\epsilon \to \infty$; the form of $f(\epsilon)$ between its limiting values depends on the slope and shape of the topography [*Garrett and Kunze*, 2007; *Dettner et al*., 2013]. The normalized power (cf. equation (4)) then is given by

$$\tilde{P}_{\text{theory}} = \frac{P_{\text{theory}}}{P_{\text{tide}}} = \frac{1}{S_{\text{IW}}} f(\epsilon). \tag{6}$$

$N(z)$ typically decreases by two orders of magnitude from the shallow ocean to the abyss (Figure 1), while equation (5) assumes that the stratification is uniform ($N = \text{const}$). To account for nonuniform stratification, *Llewellyn Smith and Young* [2002] applied the WKB approximation and found that only the stratification at the bottom boundary, $N_{\text{bot}}$, and the depth-averaged stratification, $\overline{N}$, significantly affect the generation of internal tides. *Zarroug et al*. [2010] argued that the WKB approximation yields unreliable predictions for weak stratification or for buoyancy frequency profiles that strongly vary with depth. They used homogenization theory and found that the buoyancy frequency profile should be averaged over depths comparable to the vertical length scale of the internal tide, which can significantly increase the predicted radiated power.

*King et al*. [2012] recently analyzed salinity, temperature, and pressure data for more than 18,000 locations throughout the oceans, and determined that the stratification becomes so weak in many locations that the buoyancy frequency becomes less than $\omega_{\text{M2}}$ (see example in Figure 1). As the stratification weakens and $N(z) \to \omega_{\text{M2}}$, the internal wave slope increases and becomes infinite at a turning depth $z_{\text{td}}$, where $N(z_{\text{td}}) = \omega_{\text{M2}}$ (in the absence of rotation; see *King et al*. [2012, Figure 9] for the effect of rotation on turning depths). Internal waves reflect from turning depths, and become evanescent (exponentially damped) in regions where $N(z) < \omega_{\text{M2}}$ [*Kistovich and Chashechkin*, 1998; *Paoletti and Swinney*, 2012]. Figure 1 illustrates that some topographic features peak above a turning depth, while others reside completely beneath a turning depth. Equation (5) is only applicable for cases where $\omega < N(z)$, and may not be used to predict the conversion of tidal motions to internal waves in the presence of turning depths.

## 3. Methods

### 3.1. Navier-Stokes Numerical Simulations

We numerically simulate the generation of internal waves by tidal flow over two-dimensional topography in nonuniform stratifications by solving the Navier-Stokes equations in the Boussinesq approximation using CDP 2.4 [*Ham and Iaccarino*, 2004], which is a parallel, finite-volume-based solver modeled after the algorithm of *Mahesh et al*. [2004]. We disable all subgrid scale modeling. The code utilizes a fractional-step time-marching scheme and multiple implicit schemes for the spatial operators [*Ham et al*., 2006] to achieve second-order accuracy in both space and time. We solve the following equations for the density $\rho$, pressure $p$, and velocity field $\boldsymbol{v} = (u, w)$ in the $(x, z)$ directions:

$$\frac{\partial \boldsymbol{v}}{\partial t} + (\boldsymbol{v}\cdot\nabla)\boldsymbol{v} = -\frac{1}{\rho_0}\nabla p - \frac{g\rho}{\rho_0}\hat{\mathrm{z}} + \nu\nabla^2\boldsymbol{v} + \frac{F_{\text{tide}}}{\rho_0}\hat{\mathrm{x}}, \tag{7}$$

$$\nabla\cdot\boldsymbol{v} = 0, \tag{8}$$

$$\partial\rho/\partial t + (\boldsymbol{v}\cdot\nabla)\rho = D\nabla^2\rho, \tag{9}$$

where $\rho_0 = 1000\,\mathrm{kg/m^3}$ is a reference density, $g$ is the gravitational acceleration, and $\nu = 10^{-6}\,\mathrm{m^2/s}$ is the kinematic viscosity. The salt diffusivity $D = 2 \times 10^{-9}\,\mathrm{m^2/s}$ is equal to the value for sodium chloride, which is

**Table 1.** The Topographic Shapes, Computational Domains, and Parameters Used in the Numerical Simulations[a,b]

| Run | Shape | H | $W/H$ | $x/H$ | $z/H$ | $\Delta x$ | $\Delta z$ | $N(z)$ | $\omega/N_{bot}$ | $z_{td}/H$ | $A/H$ |
|---|---|---|---|---|---|---|---|---|---|---|---|
| 1 | Knife | 50 | 0.032 | −9 to 9 | 0–9 | 0.2–0.6 | 0.3–1 | 0.99–1.87 | 0.71–1.18 | −4.8 to 2.3 | 0.02 |
| 2 | Gaussian | 50 | 3.6 | −9 to 9 | 0–9 | 1–1.5 | 0.1–1 | 0.99–1.87 | 0.71–1.18 | −4.8 to 2.3 | 0.02 |
| 3 | Gaussian | 200 | 0.45 | −40 to 40 | 0–7.5 | 0.08–90 | 0.25–1 | 0.2–2 | 0.29–3.41 | −4 to 4 | 0.005 |
| 4 | Gaussian | 200 | 1.8 | −40 to 40 | 0–7.5 | 0.3–90 | 0.25–1 | 0.2–2 | 0.29–3.41 | −4 to 4 | 0.05 |
| 5 | Gaussian | 200 | 1.8 | −40 to 40 | 0–7.5 | 0.3–90 | 0.25–1 | 0.5–1 | 0.69–1.45 | −4 to 4 | 0.02 |
| 6 | Gaussian | 200 | 1.8 | −40 to 40 | 0–7.5 | 0.3–90 | 0.25–1 | 0.5–2 | 0.48–2.09 | −4 to 4 | 0.02 |
| 7 | Gaussian | 200 | 1.8 | −40 to 40 | 0–7.5 | 0.3–90 | 0.25–1 | 0.5–5 | 0.29–3.41 | −4 to 4 | 0.005 |
| 8 | Gaussian | 200 | 1.8 | −40 to 40 | 0–7.5 | 0.3–90 | 0.25–1 | 0.5–5 | 0.29–3.41 | −4 to 4 | 0.02 |
| 9 | Gaussian | 200 | 1.8 | −40 to 40 | 0–7.5 | 0.3–90 | 0.25–1 | 0.5–5 | 0.29–3.41 | −4 to 4 | 0.05 |
| 10 | Gaussian | 200 | 1.8 | −40 to 40 | 0–7.5 | 0.3–90 | 0.25–1 | 0.5–10 | 0.30–4.94 | −3 to 4 | 0.02 |
| 11 | Gaussian | 200 | 1.8 | −40 to 40 | 0–7.5 | 0.3–90 | 0.25–1 | 2–20 | 0.29–3.41 | −4 to 4 | 0.02 |
| 12 | Gaussian | 200 | 7.2 | −40 to 40 | 0–7.5 | 1–80 | 0.25–1 | 0.2–2 | 0.29–3.41 | −4 to 4 | 0.05 |
| 13 | Gaussian | 200 | 7.2 | −40 to 40 | 0–7.5 | 1–80 | 0.25–1 | 2–20 | 0.29–3.41 | −4 to 4 | 0.05 |
| 14 | Complex | 200 | 7.2 | −40 to 40 | 0–7.5 | 0.18–80 | 0.2–1 | 0.2–2 | 0.29–3.41 | −4 to 4 | 0.005 |

[a]All lengths are in millimeters and frequencies are in rad/s.

[b]The shapes of the topography are defined by equations (13-15), $H$ is the height of the topography, $W$ is the topographic width (which we take to be $6\sigma$ for the Gaussian topography), $x/H$ ($z/H$) is the horizontal (vertical) extent of the computational domain, $\Delta x$($\Delta z$) is the horizontal (vertical) resolution, $N(z)$ is the buoyancy frequency (which varies exponentially with $z$, cf. equation (10)), $\omega/N_{bot}$ is the tidal frequency normalized by the minimum buoyancy frequency, $z_{td}$ is the turning depth height (cf. equation (12)), and $A$ is the tidal excursion.

used in the laboratory experiments described below, resulting in a Schmidt number of $\nu/D=500$. Given the large Schmidt number, the density field does not mix through diffusion over the course of our simulations or experiments; further, no overturning or wave breaking is observed for the parameter values that we have examined.

The tidal flow $\boldsymbol{u}_{tide}=-\hat{x}A\omega\cos\omega t$ is driven by the tidal force $F_{tide}=\rho_0 A\omega^2\sin\omega t$, where $A$ is the tidal excursion. We vary the turning depth $z_{td}$ by changing the tidal frequency $\omega$; we find that the results obtained in this way are indistinguishable from those obtained by varying the stratification with the tidal frequency fixed.

No-slip boundary conditions are applied along the upper and lower boundaries, and periodic boundary conditions are used in the $x$ direction. We minimize finite-size effects by applying a Rayleigh damping force proportional to the deviation from the background tidal velocity $(\propto(\boldsymbol{v}-\boldsymbol{u}_{tide}))$ near the boundaries in the $x$ direction.

The Reynolds number based upon the tidal flow and topographic height, $Re=A\omega H/\nu$, ranges from 45 to 13,600, while the topographic Froude number, $Fr=A\omega/N_{bot}H$, spans $10^{-3}-10^{-1}$. The time step is chosen to yield either 1000, 1500, 2000, or 2500 time steps per period, depending upon the parameters of the simulation (fewer time steps are required for cases where the topography is beneath a turning depth). The simulations are run long enough to yield a steady state for at least three periods for averaging purposes; this typically requires at least 20 tidal periods.

We use an exponential buoyancy frequency profile to model the deep ocean [*King et al.*, 2012; *Paoletti and Swinney*, 2012],

$$N(z)=N_{bot}\exp\left[(z-z_{bot})/\Lambda\right],\ \text{for}\ z_{bot}\le z\le z_{top}. \tag{10}$$

The stratification length scale is

$$\Lambda=(z_{top}-z_{bot})/\ln(N_{top}/N_{bot}), \tag{11}$$

where $z_{top}=\max(z)$ is the maximum height, $N_{top}=N(z_{top})$ is the maximum buoyancy frequency, $z_{bot}=\min(z)$ is the bottom boundary, and $N_{bot}=N(z_{bot})$ is the minimum buoyancy frequency. The range of buoyancy frequencies used in the numerical simulations is listed in Table 1.

The turning depth height $z_{td}$ is defined by $N(z_{td})=\omega$. Given the stratification (10), we have

$$z_{td}=\Lambda\ln(\omega/N_{bot})+z_{bot}. \tag{12}$$

For cases where $\omega>N_{bot}$, the turning depth has a positive value and part of the topography resides beneath the turning depth, as in the example shown in Figure 1. Even though there is no turning depth

when $\omega < N_{bot}$, we characterize the strength of the stratification by allowing $z_{td}$ to be negative, with more negative values indicating a stronger stratification. The range of turning depth heights examined is given in Table 1.

### 3.2. Topography and Computational Domains

The computational domains are listed in Table 1. Simulations are compared to experiments for a domain that is 900 mm wide and 450 mm tall with $1.4 \times 10^6$ control volumes. A domain that is 16 m wide and 1.5 m tall with approximately $3 \times 10^6$ control volumes is used for additional parameter exploration. Structured grids are generated using Pointwise Gridgen (http://www.pointwise.com). The spatial resolution decreases smoothly from the highest resolution along the topography to the lowest resolution at the domain boundaries (see Table 1). Convergence tests with the spatial and temporal resolution doubled (halved) change the computed velocities by $<1\%$ (4%).

We use three different topographic shapes: a knife edge, Gaussian, and complex topography. The knife edge is approximated by a narrow top hat,

$$h_{\text{knife}}(x) = \begin{cases} H & : |x| \le W/2 \\ 0 & : |x| > W/2 \end{cases} \tag{13}$$

which results in an infinite topographic slope. The Gaussian topography is given by

$$h_{\text{gauss}}(x) = H \exp\left(-x^2/2\sigma^2\right), \tag{14}$$

where we take the width of the topography to be $W = 6\sigma$ (since the topography decays to 1% of its maximum height at $|x| = 3\sigma$). We consider cases where the maximum topographic slope of the Gaussian ridge is $S_{\text{topo}} = \{0.5, 1, 2, 8\}$. The complex topography is composed of a Gaussian envelope that is modulated by sinusoidal variations over the range $|x| < 1$m:

$$h_{\text{complex}}(x) = \begin{array}{c} 16.715 \exp\left(-x^2/3200\right) \\ \times \quad |0.25 \sin(0.52x) + \cos(0.115x)|, \end{array} \tag{15}$$

where the tallest peak has a height $H = 200$ mm and the maximum topographic slope is approximately 4.

### 3.3. Radiated Power

The far-field radiated power in the internal tide is obtained by integrating the energy flux field normal to a cross section that contains the topography (see equation (1)). We choose a cross section that extends vertically from the base of the domain at $x = \pm 5H$ up to $z = 1.3H$ and then extends horizontally from $x = -5H$ to $x = 5H$ at $z = 1.3H$. Thus, the radiated power is given by

$$\begin{aligned} P_{\text{IW}} = &\int_0^{1.3H} \mathbf{\Phi}(x = -5H, z) \cdot (-\hat{\mathrm{x}}) dz \\ &+ \int_0^{1.3H} \mathbf{\Phi}(x = 5H, z) \cdot (\hat{\mathrm{x}}) dz \\ &+ \int_{-5H}^{5H} \mathbf{\Phi}(x, z = 1.3H) \cdot (\hat{\mathrm{z}}) dx, \end{aligned} \tag{16}$$

where the energy flux is given by

$$\mathbf{\Phi} = \langle p' [(u - u_{\text{tide}})\hat{\mathrm{x}} + w\hat{\mathrm{z}}] \rangle, \tag{17}$$

where the brackets $\langle\rangle$ indicate averages over three tidal periods. The qualitative behavior of the radiated power does not depend on the particular choice of the cross section [*Dettner et al.*, 2013] or the relative distance between the cross section and the turning depth. The power monotonically decreases because of viscous dissipation as the distance between the cross section and the topography increases, as Figure 4b shows. Our choice in cross section approximately minimizes near-field effects, which arise when the cross

section is too near the topography, and viscous effects, which increase as the cross section moves away from the topography.

### 3.4. Experimental Techniques

We perform laboratory experiments in a glass tank that spans $-450 < x < 450\,\text{mm}$, $0 < y < 450\,\text{mm}$, and $0 < z < 600\,\text{mm}$. Exponential density profiles are generated using the generalized double bucket method described by *Hill* [2002]. We extract fluid samples at known heights and measure the density of each with an Anton Paar density meter. The total fluid depth is 550 mm, and the density profile is well described by

$$\rho_{\text{expt}} = 127\exp(-0.00282z) + 971\,(\text{kg/m}^3), \tag{18}$$

over the range $0 < z < 500\,\text{mm}$. The topography is inverted with its base set at $z = 450\,\text{mm}$. Thus, given the stratification (18), the buoyancy frequency at the base of the experimental topography is $N_{\text{bot}} = 0.99\,\text{rad/s}$ and the maximum buoyancy frequency is 1.87 rad/s, as in runs 1 and 2 described in Table 1.

The knife edge or Gaussian ridge has height $H = 50$ mm, centered at $x = 0$, and spans the tank in the $y$ direction. The knife edge has a width of $W = 0.032H$ and the Gaussian has $W = 3.6H$, thus matching the parameters of the first two series of simulations (cf. Table 1). The knife edge topography is connected to a base that spans $-394 < x < 394\,\text{mm}$, $10 < y < 440\,\text{mm}$, and $450 < z < 462.7\,\text{mm}$, to emulate a no-slip bottom boundary condition. The Gaussian topography is connected to a similar base that spans the same range in the $x$ and $y$ directions, and in the $z$ direction it spans $450 < z < 456.4\,\text{mm}$. The edges of the base plates at $|x| = 394\,\text{mm}$ are rounded to reduce the spurious generation of internal tides from the ends.

Tidal flow is simulated by oscillating the topography and the base plate, rather than driving the fluid over stationary topography. Our experimental measurements are therefore in a reference frame that moves with the tidal flow. The position of the topography is given by

$$x(t) = A[1 - \exp(-2\omega t/3\pi)]\sin(\omega t), \tag{19}$$

where the tidal excursion is fixed at $A = 1$ mm. The tidal frequency is varied over the range $0.7 < \omega < 1.17\,\text{rad/s}$ to change the height of the turning depth $z_{\text{td}}$. The exponential term in (19) is added to gradually increase the oscillation amplitude, which reaches 99% of its peak value after approximately 3.5 tidal periods [*Echeverri et al.*, 2009]. The Reynolds number $Re = A\omega H/\nu$ based upon the topographic height and tidal flow is approximately 50. The end walls at $|x| = 450\,\text{mm}$ are lined with fiber mesh to reduce reflections.

Two-dimensional velocity fields $\boldsymbol{v} = (u, w)$ are obtained by particle image velocimetry in a vertical plane along the center of the tank at $y = 225\,\text{mm}$. Hollow glass spheres with densities $1050 < \rho < 1150\,\text{kg/m}^3$ and diameters $8 < d < 12$ $\mu$m are used as seed particles, which are illuminated by a 5 mm thick laser sheet produced by a 532 nm wavelength laser (2 W). The tracer particle motions are captured 20 times per period by two 12 bit CCD cameras with $1296 \times 966$ pixel resolution, each imaging a 152.5 mm $\times$ 113.6 mm region. The cameras are separated by 122.5 mm in the $x$ direction so that their measurement regions overlap by approximately 30 mm, thereby yielding a combined field of view of 272.5 mm $\times$ 113.6 mm. We use the CIV algorithm developed by *Fincham and Delerce* [2000] to determine the instantaneous velocity field, which is interpolated to a regular $200 \times 100$ grid with spatial resolutions of $\Delta x = 1.3\,\text{mm}$ and $\Delta z = 1.1\,\text{mm}$.

We compare the experimental measurements to the computations for the 50 mm tall knife edge and Gaussian topographies to verify the numerical simulations, as in our prior studies using the CDP code [*King et al.*, 2009, 2010; *Paoletti and Swinney*, 2012]. Figure 2 illustrates the remarkable agreement obtained between the numerical simulations and the laboratory experiments, both in the presence and the absence of a turning depth. For both the knife edge and Gaussian topographies, we find similar agreement between the experiments and simulations for different tidal frequencies, spatial locations, and phases of the tidal cycle.

## 4. Results

### 4.1. Dependence of the Power in the Internal Tides on Turning Depth

Figure 3 illustrates our main results: (*i*) topography completely beneath a turning depth ($z_{\text{td}} > H$) still converts barotropic tidal motions to internal wave radiation and the turning depth and (*ii*) turning depths

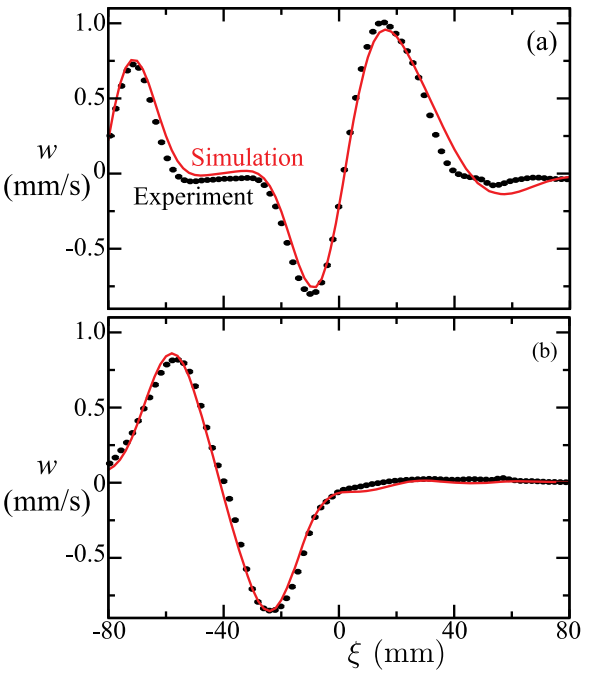


**Figure 2.** Measurements of the vertical velocity component (black circles) along a horizontal cross section (100 mm away from the peak of the knife edge) at an instant of time agree well with numerical simulations (red curves) for the full parameter ranges investigated, as illustrated here for cases (a) with a turning depth beneath the topography, $z_{td}/H = -0.47$ and $\omega/\min(N) = 0.97$ and (b) with a turning depth above the topography, $z_{td}/H = 1.46$ and $\omega/\min(N) = 1.11$ (knife edge topography with $H = 50$ mm and $0.99 < N(z) < 1.87 \mathrm{rad/s}$).

greatly reduce the radiated power of the internal wave beams compared to cases where turning depths are absent ($z_{td} < 0$). We characterize the energy flux by

$$\Phi_{IW} \equiv \mathbf{\Phi} \cdot \hat{z}/\sin(\theta), \qquad (20)$$

which has a magnitude equal to the magnitude of the energy flux in the direction of propagation and a sign that is positive (negative) for upward (downward) propagating internal wave beams. The peak values of $\Phi_{IW}$ are far weaker when a turning depth lies above the topography than when there is no turning depth. For example, in Figure 3c, the turning depth is at twice the maximum height of the topography and the peak of $\Phi_{IW}$ is two orders of magnitude weaker than when there is no turning depth (Figure 3a); in the latter case the tidal conversion is strong enough to generate the second harmonic.

Nonuniform stratification can intensify the energy flux as a result of the varying angle of propagation. For the case of $z_{td}/H = 0$, the energy flux $\Phi_{IW}$ through a vertical cross section near the topography ($x/H = 1$) is bimodal, however it becomes unimodal and intensified near $x/H = 8$ (Figure 4a). Even though the peak values of the energy flux may increase as the internal wave beam propagates away from the topography, the total radiated power $P_{IW}$ (given by the integrated energy flux) monotonically decreases owing to viscous attenuation (Figure 4b). While nonuniform stratification can affect the local values of the energy flux, the radiated power is fully determined by the power generated by the topography and by viscous attenuation.

The focusing of energy flux from nonuniform stratification increases with an increase in $N_{top}/N_{bot}$, the ratio of the maximum to minimum buoyancy frequency. For the cases shown in Figure 4, $N_{top}/N_{bot} = 10$, while in the ocean the buoyancy frequency varies by more than two orders of magnitude (see Figure 1). We therefore expect such focusing to be much stronger for oceanic internal tides.

We use equation (16) to compute the total radiated power in the internal wave beams. Figures 5a and 5b show that the higher the turning depth relative to the topographic height, $z_{td}/H$, the lower the normalized radiated internal wave power, and this trend holds regardless of the width of the topography (Figure 5a) or the range of variation in $N(z)$ (Figure 5b). The normalized power is unchanged for an increase in tidal excursion from $A/H = 0.005$ to $A/H = 0.05$, which indicates that nonlinear effects are weak for the range of parameters that we have explored.

### 4.2. Variation With Topographic Width

Many prior studies have focused on the scaling of the radiated power with the criticality parameter $\epsilon = S_{topo}/S_{IW}$, as reviewed by *Garrett and Kunze* [2007]. Those studies found that the radiated power smoothly increases only by a factor of 2 as $\epsilon$ increases from values near zero to $\epsilon \to \infty$ [*Pétrélis et al.*, 2006]. Thus for fixed height topography, the radiated power is predicted to increase as the width of the topography decreases.

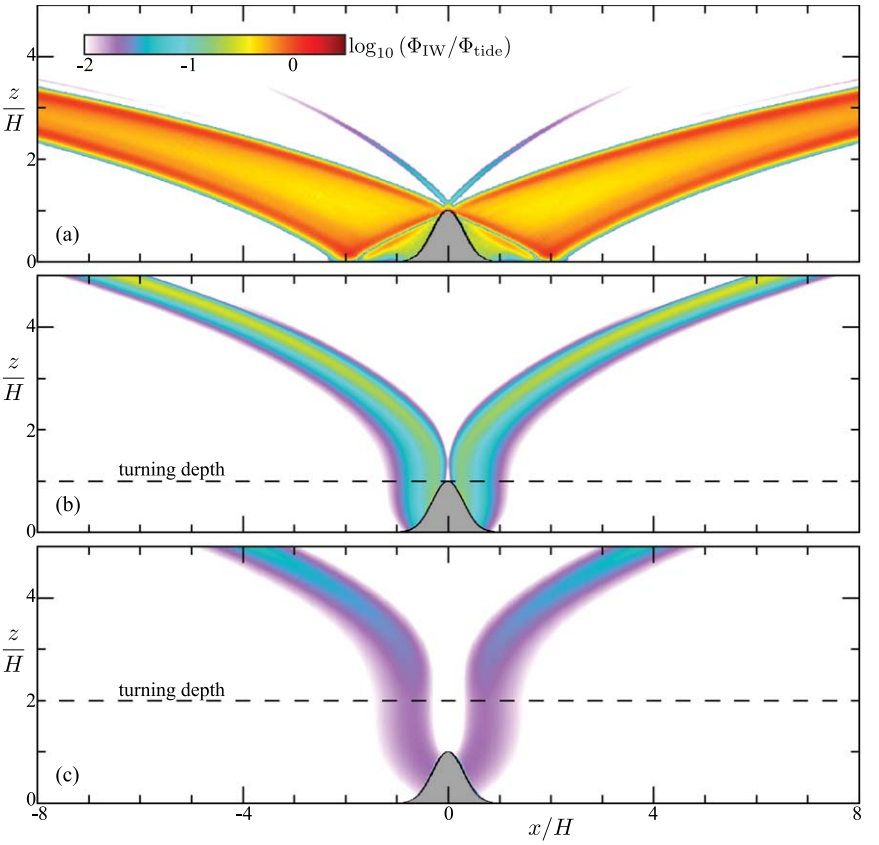


**Figure 3.** Intense internal waves are generated when the turning depth is below the topography (a) $z_{td}/H=-2$, as compared to turning depths (b) at the top of the topography, $z_{td}/H=1$, and (c) above the topography, $z_{td}/H=2$. The tidally averaged energy flux in the direction of propagation, $\Phi_{IW}$ (see color bar), is normalized by the tidal energy flux $\Phi_{tide}$, with $H=200\text{mm}$, $W/H=1.8$, $A/H=0.02$, and $\omega/N_{bot}$ = (a) 0.51, (b) 1, and (c) 1.85; $0.5 < N(z) < 5\text{rad/s}$.

Figure 5a compares the normalized power for Gaussian topography with three topographic slopes, $S_{topo} = 0.5$, 2, and 8. For cases without a turning depth $(z_{td}/H < 0)$, the narrower ridges produce more internal wave power owing to their greater topographic slopes and criticality parameters, as expected from theory. As the stratification becomes stronger $(z_{td}/H \to -4)$, the internal wave slopes become shallow compared to the slope of all three Gaussian ridges, rendering the differences in the topographic slopes

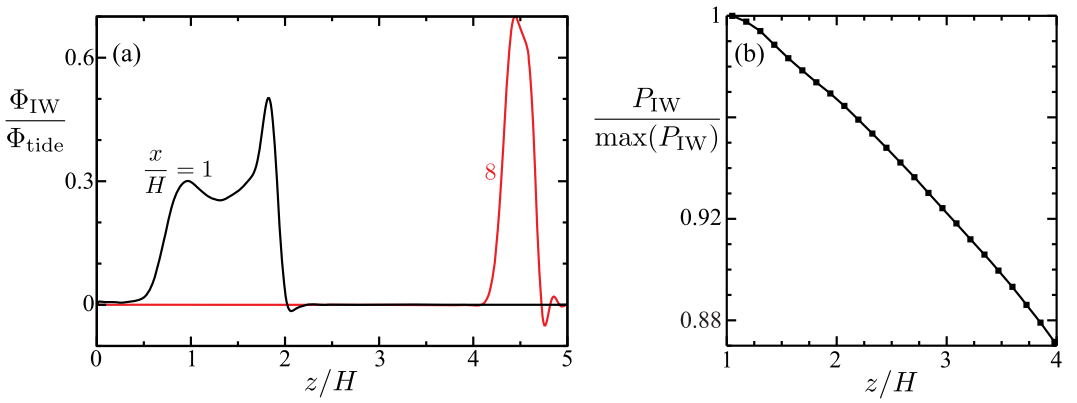


**Figure 4.** (a) The peak tidally averaged energy flux in the direction of propagation, $\Phi_{IW}$ (normalized by the maximum tidal energy flux $\Phi_{tide}$), increases as the internal waves propagate into stronger stratification (increasing $z$), and the two beams merge into a single beam because of focusing by the strong stratification: the cross section at $x/H=1$ (black curve) has two peaks, while at $x/H=8$ there is a single peak (red curve). (b) The total radiated power decreases monotonically with distance, even though the peak energy flux increases. (Gaussian topography with $H=200\text{mm}$, $W/H=1.8$, $A/H=0.02$, $z_{td}/H=0$, and $0.5 < N(z) < 5\text{rad/s}$.)

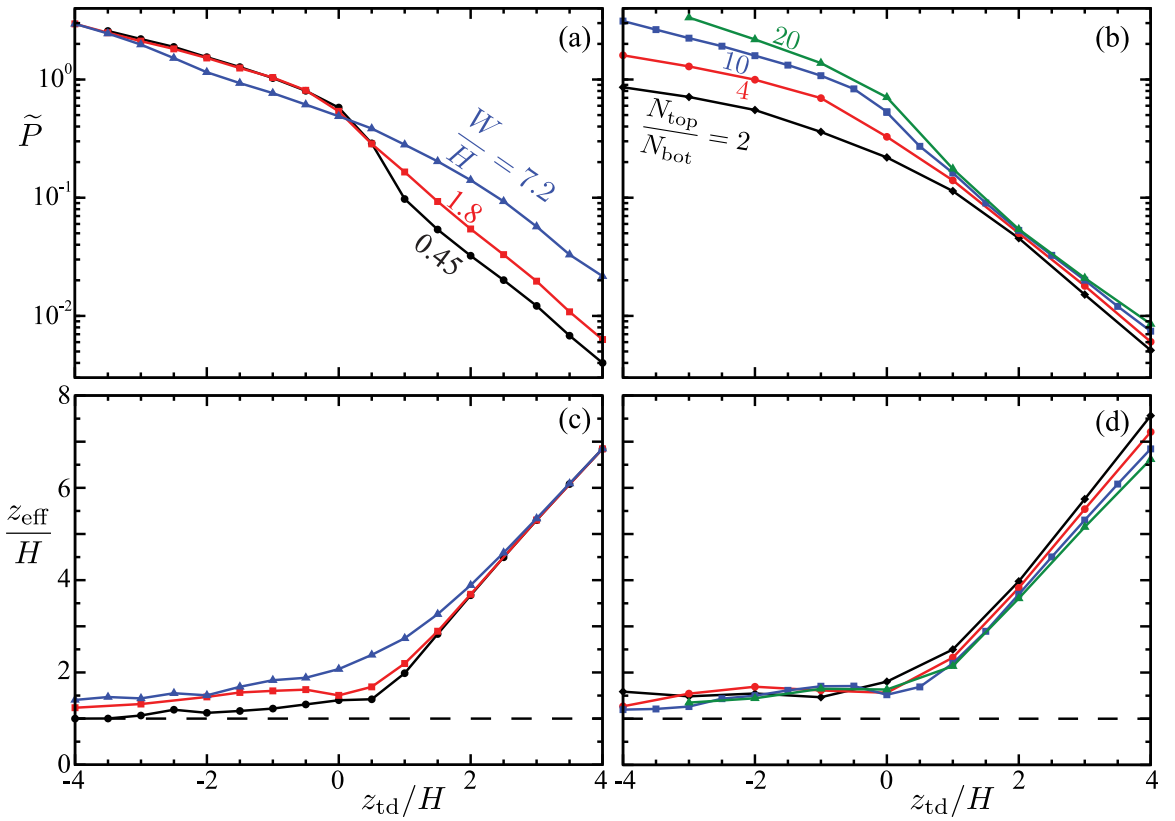


**Figure 5.** The radiated internal wave power $\tilde{P}$ (normalized as in equation (4)) decreases with increasing turning depth height $z_{td}$, as illustrated in (a) for Gaussian topographies of different widths and in (b) for different buoyancy frequency ratios $N_{top}/N_{bot}$ (where the maximum buoyancy frequency $N_{top}$ is varied and the minimum $N_{bot}$ is fixed). Further, in the presence of turning depths Figure 5a shows that the radiated power is larger for wider topography and Figure 5b shows that the radiated power only weakly increases for larger $N_{top}/N_{bot}$ ratios. (c and d) in the absence of a turning depth ($z_{td}/H < 0$), the effective height $z_{eff}$ over which the stratification must be averaged to yield the measured radiated power (see equations (21-23)) is approximately equal to the topographic height, but for increasing turning depth heights $z_{td}/H$, the averaging must be done over heights increasing toward the height of the domain (7.5$H$); this behavior depends only weakly on $W/H$, as Figure 5c illustrates, and weakly on $N_{top}/N_{bot}$, as Figure 5d illustrates. In these simulations, $H = 200$ mm, tidal excursion $A/H$=0.005, and $N_{bot}$ =0.5rad/s .

negligible and resulting in approximately the same normalized power. The internal wave slope diverges as $z_{td} \to 0$; hence the radiated power again becomes independent of the topographic width, in accord with the analytical predictions of *Bell* [1975b]. However, unlike cases without a turning depth, the widest topography most strongly converts tidal motions into internal tides for $z_{td}/H > 0$ (Figure 5a). The value of $\tilde{P} \approx 2$ for $z_{td}/H = -4$ stems from the particular choice in stratification and is not uniquely determined by $z_{td}$ (see section 4.3). In fact, in the limit of $z_{td}/H \to -\infty$, which corresponds to $N \to \infty$, the normalized power $\tilde{P} \to \infty$.

### 4.3. Role of Stratification

The normalized power does not vary if we increase $N_{bot}$ for fixed $N_{top}/N_{bot}$. This indicates that the *efficiency* of the conversion of tidal motions to internal waves is independent of $N_{bot}$ for fixed $z_{td}$. Increasing the stratification over the entire water column does result in more dimensional power in the internal waves, as increasing $N_{bot}$ for fixed $z_{td}$ increases $\omega$ by the same factor (cf. equations (4) and (12)). This increase in tidal frequency results in a corresponding increase in the tidal velocities and radiated power, as predicted by equation (5).

*Llewellyn Smith and Young* [2002] used the WKB approximation to account for nonuniform stratifications, finding that the generation of internal waves was affected by the depth-averaged stratification $\bar{N}$, in addition to the bottom-boundary buoyancy frequency $N_{bot}$. The effect of varying the depth-averaged stratification $\bar{N}$ on the normalized power $\tilde{P}$ is illustrated in Figure 5b, where $\bar{N}$ is increased by decreasing the stratification length scale $\Lambda$ (cf. (10) and (11)); this increases the maximum buoyancy frequency $N_{top}$ for fixed $N_{bot}$. Increasing $\bar{N}$ results in larger values of normalized power, particularly in the absence of turning

depths (negative values of $z_{td}$). The normalized power varies weakly with $N_{top}/N_{bot}$ in the presence of turning depths ($z_{td}/H > 0$). For example, the normalized power increases by a factor of 4 for an order of magnitude increase in $N_{top}/N_{bot}$ (from 2 to 20) when the turning depth is beneath the topography at $z_{td}/H = -2$. However, when $z_{td}/H = 2$, for the same increase in $N_{top}/N_{bot}$ the power only changes by 20%.

### 4.4. Effective (Average) Stratification

We have demonstrated that topography beneath a turning depth can convert tidal motions into far-field internal wave power. *Zarroug et al*. [2010] argued that the WKB approximation, which is often used to analyze nonuniform stratifications, is unreliable for small values of $N_{bot}$ or when the stratification varies strongly with depth. They argue that the stratification should be averaged over depths comparable to the vertical length scale of the internal wave beam. Figure 3 illustrates that the vertical length scale of the internal waves increases with increasing turning depth height, thereby shifting the modal content to lower modes. *Zarroug et al*. [2010] argued that for the lowest modes, the effective stratification should be obtained by averaging over the entire fluid depth, which leads to radiated powers that can far exceed those estimated using the WKB approximation. Along similar lines, *Qian et al*. [2010] found in numerical simulations that the presence of a pycnocline above the topography enhanced the generation of internal tides and could be interpreted as producing a larger criticality parameter $\epsilon_{eff}$.

These past studies indicate that the stratification above the topography must be taken into account when predicting the internal wave power. This leads us to modify equation (5) for a uniformly stratified fluid to account for the stratification from the bottom boundary to an effective height $z_{eff}$, which will depend upon the details of the topography and stratification:

$$P_{eff} = \rho_0 H^2 A^2 \omega^2 \sqrt{N_{eff}^2 - \omega^2} f(\epsilon_{eff}), \tag{21}$$

where an effective uniform stratification is given by

$$N_{eff} = \frac{1}{z_{eff}} \int_0^{z_{eff}} N(z) \mathrm{d}z. \tag{22}$$

The effective stratification yields an effective criticality parameter given by

$$\epsilon_{eff} = S_{topo} \frac{\sqrt{N_{eff}^2 - \omega^2}}{\omega}. \tag{23}$$

The function $f(\epsilon_{eff})$ smoothly varies from $f(\epsilon_{eff} \to 0) = \pi/8$ to $f(\epsilon_{eff} \to \infty) = \pi/4$ for an isolated ridge. A number of studies [*Balmforth et al*., 2002; *Pétrélis et al*., 2006; *di Lorenzo et al*., 2006; *Garrett and Kunze*, 2007; *Echeverri and Peacock*, 2010; *Dettner et al*., 2013] have shown that the variation of $f(\epsilon_{eff})$ between the upper and lower bounds depends upon the shape and slope of the topography. *Qian et al*. [2010] averaged the stratification over the depths spanned by the ridge, which in our notation corresponds to $z_{eff} = H$.

We determine the effective height $z_{eff}$ iteratively: we first assume that $\epsilon_{eff}$ is initially determined by equation (23) with $N_{eff} = N_{bot}$, which allows us to estimate $f(\epsilon_{eff})$ from the results of *Dettner et al*. [2013]. Then we make an initial estimate of $N_{eff}$ by inverting equation (21) using our measured value of $P_{IW}$ for $P_{eff}$ and our initial estimate of $f(\epsilon_{eff})$. We then use the first estimate of $N_{eff}$ to update $\epsilon_{eff}$, which modifies the value of $f(\epsilon_{eff})$ used in equation (21). With a new value of $f(\epsilon_{eff})$, we determine an updated value of $N_{eff}$ from equation (21), again using the measured value of $P_{IW}$ for $P_{eff}$. This process continues until the change in the value of $\epsilon_{eff}$ is less than a predetermined threshold; we halt the procedure once the change in $\epsilon$ is $<0.02$, although the results are not particularly sensitive to the choice in the threshold value.

Figures 5c and 5d show our results for the effective height $z_{eff}$ corresponding to the normalized power shown in Figures 5a and 5b, respectively. In the absence of a turning depth ($z_{td}/H < 0$), the effective height is only slightly larger than the topographic height $H$, with wider topography yielding larger values than narrower topography. Even though the normalized power varies as the ratio $N_{top}/N_{bot}$ is varied (Figure 5b) in the absence of a turning depth, $z_{eff}$ does not change, which indicates that the larger values of $\tilde{P}$ for increasing buoyancy frequency ratio stem from the stronger stratification only over the depths spanned by the

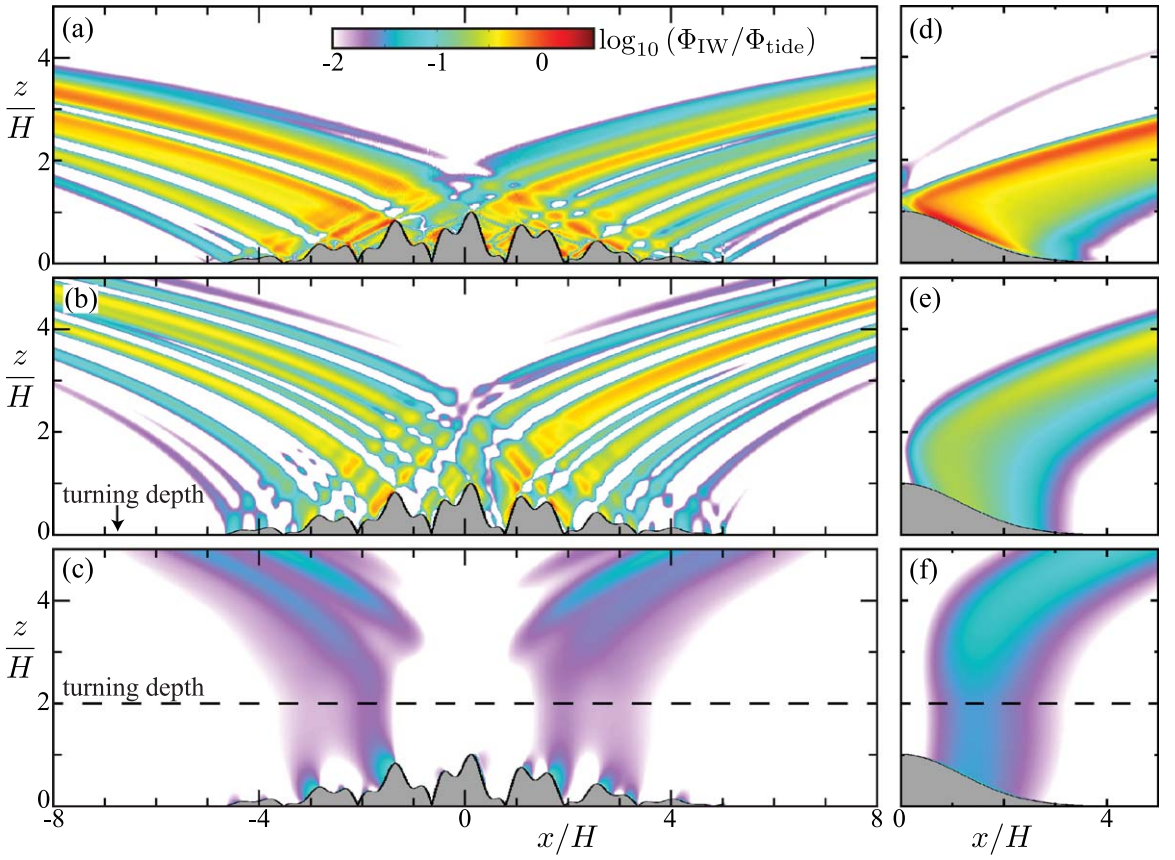


**Figure 6.** The internal wave structure generated by tidal motions over (a–c) complex topography is more complex than the corresponding cases with (d–f) Gaussian topography. Intense internal waves are generated when the turning depth is below the topography, $z_{td}/H=-2$ (Figures 6a and 6d), compared to cases where the turning depth is at the bottom of the topography, $z_{td}/H=0$ (Figures 6b and 6e), or above the topography, $z_{td}/H=2$ (Figures 6c and 6f). The tidally averaged energy flux in the direction of the propagation, $\Phi_{IW}$ (color), is normalized by the maximum tidal energy flux $\Phi_{tide}=\rho_0 A^2\omega^3 H$, where $H=200$mm , $A/H=0.005$, and $\omega/N_{bot}=$ (a) 0.51, (b) 1, and (c) 1.85 for $0.2<N(z)<2$rad/s . The shape of the complex topography is given in equation (15).

topography, as $z_{eff}\approx H$. However, in the presence of a turning depth, $z_{eff}$ increases approximately linearly toward values near the depth of the water column $(z/H=7.5)$. Thus, the stratification over the entire fluid depth is relevant for the weakest stratifications, in accordance with the arguments of *Zarroug et al.* [2010]. The change in behavior of $z_{eff}$ from being roughly constant for $z_{td}/H<0$ to linearly increasing for $z_{td}/H>1$ is only weakly dependent on topographic width (Figure 5c) and buoyancy frequency ratio (Figure 5d).

We interpret $z_{eff}$ to indicate the vertical length scale of the internal waves, as suggested by *Zarroug et al.* [2010]. If this vertical length scale is less than or comparable to the topographic height $H$, then we expect that the radiated power will be determined by the average stratification over depths spanned by the topography. We observe this to be the case in the absence of turning depths, as Figures 5c and 5d show that $z_{eff}\approx H$. Furthermore, $z_{eff}$ for the widest topography is always larger than for narrower topography, which is expected given that wider topography generates internal waves with larger length scales. In the presence of turning depths that extend above the topography $(z_{td}/H>1)$, the stratification in the vicinity of the topography is too weak to support the internal tide. Thus, the vertical scale of the internal wave field extends into regions farther above the topography where the stratification is stronger, which explains the monotonic increase in $z_{eff}$ with increasing $z_{td}$ in the presence of turning depths. This behavior is qualitatively shown in Figure 3, where the internal wave beams are narrow and sharply peaked for $z_{td}/H=-2$ (plot a), while only a single broad beam is generated for $z_{td}/H=2$ (plot c).

### 4.5. Complex Topography

To go beyond simple Gaussian topography toward the topography of the ocean, we now consider tidal conversion by the complex two-dimensional topography given by equation (15). (Of course equation (15)

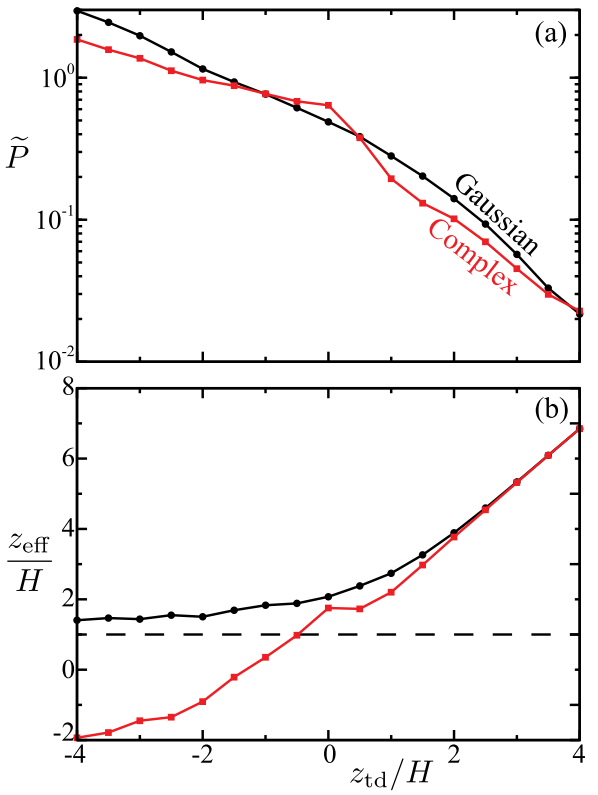


**Figure 7.** (a) The normalized power radiated by complex (red squares) and Gaussian (black circles) two-dimensional topographies with the same area exhibit a similar dependence on turning depth height $z_{td}/H$. (b) The effective height over which the stratification must be averaged to yield the corresponding radiated power behaves similarly for both Gaussian and complex topographies for large $z_{td}/H$. However, for stronger stratification ($z_{td}/H < 0$), the effective height tends toward $H$ (dashed line) for Gaussian topography, but decreases to negative values for complex topography, owing to the reduction in radiated power arising from interference.

provides only a single example of complex topography. Statistically significant statements about internal wave power generation in the world's oceans would require a large number of realizations of random topography satisfying the oceanic topographic spectrum [*Melet et al.*, 2013].) Figure 6 compares the internal wave energy flux fields generated by the complex topography to cases with Gaussian topography of the same maximum height and approximately the same cross-sectional area. The complex topography clearly generates more complicated energy flux fields, because interference leads to regions of intense energy flux as well as voids with weak flux. For increasing turning depth heights, the energy flux fields generated by the complex topography and Gaussian topography become increasingly similar (cf. Figures 6c and 6f).

For both the complex and Gaussian topographies, the normalized radiated power decreases with increasing $z_{td}$ (Figure 7a). For strong stratification ($z_{td}/H \to -4$), the Gaussian topography radiates more power than the complex topography, even though the maximum slope of the complex topography is eight times larger than that of the Gaussian topography. When the turning depth is near the base of the topography ($z_{td}/H=0$), the power radiated by the complex topography slightly exceeds that of the Gaussian ridge, despite the large areas with negligible energy flux caused by interference in the case of the complex topography (compare Figures 6b and 6e). Once the turning depth completely envelops the ridges ($z_{td}/H > 1$), the Gaussian topography again yields more power than the complex topography, but the disparity decreases with increasing $z_{td}$.

The effective heights $z_{eff}$ computed from equations (21-23) are very similar for $z_{td}/H > 2$, indicating that the details of the topography are unimportant for turning depths above the topography. However, for $z_{td}/H < 0$, the effective height tends toward the topographic height for Gaussian topography, whereas for complex topography $z_{td}$ becomes negative, indicating that the radiated power is significantly weaker than the power radiated by an isolated ridge of the same height and maximum slope. This is in accord with prior studies [*Khatiwala*, 2003; *Nycander*, 2006; *Balmforth and Peacock*, 2009], which found that interference can reduce the power generated by multipeaked or periodic topography. An explanation for this reduction in power is provided by the virtual ocean floor model presented by *Zhang and Swinney* [2014].

## 5. Discussion

Our numerical simulations show that topography beneath a turning depth (e.g., see Figure 1) converts barotropic tidal motions to weak baroclinic internal tides that radiate to the far-field. Internal tides generated by topography beneath a turning depth have weak destabilizing shear because the wave spatial scale is larger than when turning depths are absent. However, the internal tides may still break and mix as a consequence of focusing as the beams propagate from the abyss into stronger stratifications (cf. Figure 4). Steeper

topography generates stronger internal tides than shallow topography in the absence of a turning depth, but the opposite is true for topography beneath a turning depth. The radiation from complex and Gaussian topographies below a turning depth is similar, but in the absence of a turning depth Gaussian topography is more efficient in generating internal tides.

In the absence of turning depths, we find that prior theoretical results [*Bell*, 1975b; *Balmforth et al*., 2002; *Llewellyn Smith and Young*, 2003; *Garrett and Kunze*, 2007; *Echeverri and Peacock*, 2010] yield good estimates of our measured radiated powers if the stratification is averaged over depths spanned by the topography. However, we find that in the presence of turning depths the vertical scales of the internal waves increase, and the stratification must be averaged over a larger effective height, $z_{\mathrm{eff}}$, to obtain the radiated power; $z_{\mathrm{eff}}$ increases approximately linearly with turning depth height for topography of different shapes, widths, and buoyancy frequency changes from the bottom to $z_{\mathrm{eff}}$. For very weak stratifications, the vertical length scales of the internal tides increase to the point that the effective height approaches the height of the water column, in accord with the theory developed by *Zarroug et al*. [2010].

The present work has focused on the generation of internal waves by tidal flow over two-dimensional topography in an exponentially stratified fluid in a deep ocean. In the real ocean, three-dimensional and rotational effects play a role in mixing by reflecting and scattering of internal waves [*Gemmrich and van Haren*, 2001; *Garrett and St. Laurent*, 2002]. Future work should examine three-dimensional and rotational effects on wave generation, reflection, and scattering in a deep nonuniformly stratified ocean with a turning depth.

**Acknowledgments**
We thank Likun Zhang, Bruce Rodenborn, Philip Morrison, and Robert Moser for helpful discussions. The computations were done at the Texas Advanced Computing Center. The research was supported by the Office of Naval Research MURI grant N000141110701.

## References

Baines, P. (1973), The generation of internal tides by flat-bump topography, *Deep Sea Res. Oceanogr. Abstr.*, *20*(2), 179–205, doi:10.1016/0011-7471(73)90050-8.

Balmforth, N. J., and T. Peacock (2009), Tidal conversion by supercritical topography, *J. Phys. Oceanogr.*, *39*, 1965–1974, doi:10.1175/2009JPO4057.1.

Balmforth, N. J., G. R. Ierley, and W. R. Young (2002), Tidal conversion by subcritical topography, *J. Phys. Oceanogr.*, *32*, 2900–2914, doi:10.1175/1520-0485(2002)032¡2900:TCBST¿2.0.CO;2.

Bell, T. H. (1975a), Lee waves in stratified flows with simple harmonic time dependence, *J. Fluid Mech.*, *67*, 705–722, doi:10.1017/S0022112075000560.

Bell, T. H., Jr. (1975b), Topographically generated internal waves in the open ocean, *J. Geophys. Res.*, *80*, 320–327, doi:10.1029/JC080i003p00320.

Cacchione, D. A., L. F. Pratson, and A. S. Ogston (2002), The shaping of continental slopes by internal tides, *Science*, *296*, 724–727, doi:10.1126/science.1069803.

Dettner, A., M. S. Paoletti, and H. L. Swinney (2013), Internal wave and boundary current generation by tidal flow over topography, *Phys. Fluids*, *25*, 116,601.

di Lorenzo, E., W. R. Young, and S. G. Llewellyn Smith (2006), Numerical and analytical estimates of M2 tidal conversion at steep oceanic ridges, *J. Phys. Oceanogr.*, *36*, 1072–1084, doi:10.1175/JPO2880.1.

Echeverri, P., and T. Peacock (2010), Internal tide generation by arbitrary two-dimensional topography, *J. Fluid Mech.*, *659*, 247–266, doi:10.1017/S0022112010002417.

Echeverri, P., M. R. Flynn, K. B. Winters, and T. Peacock (2009), Low-mode internal tide generation by topography: An experimental and numerical investigation, *J. Fluid Mech.*, *636*, 91–108, doi:10.1017/S0022112009007654.

Fincham, A., and G. Delerce (2000), Advanced optimization of correlation imaging velocimetry algorithms, *Exp. Fluids*, *29*, 13–22.

Garrett, C., and E. Kunze (2007), Internal tide generation in the deep ocean, *Annu. Rev. Fluid Mech.*, *39*, 57–87, doi:10.1146/annurev.fluid.39.050905.110227.

Garrett, C., and L. St. Laurent (2002), Aspects of deep ocean mixing, *J. Oceanogr.*, *58*, 11–24.

Gemmrich, J. R., and H. van Haren (2001), Thermal fronts generated by internal waves propagating obliquely along the continental slope, *J. Phys. Oceanogr.*, *31*, 649–655, doi:10.1175/1520-0485(2001)031¡0649:TFGBIW¿2.0.CO;2.

Ham, F., and G. Iaccarino (2004), Energy conservation in collocated discretization schemes on unstructured meshes, in *Annual Research Briefs*, pp. 3–14, Cent. for Turbulence Res., Stanford, Calif.

Ham, F., K. Mattsson, and G. Iaccarino (2006), Accurate and stable finite volume operators for unstructured flow solvers, in *Annual Research Briefs*, pp. 243–261, Cent. for Turbulence Res., Stanford, Calif.

Hill, D. F. (2002), General density gradients in general domains: The "two-tank" method revisited, *Exp. Fluids*, *32*, 434–440.

Hurley, D. G., and G. Keady (1997), The generation of internal waves by vibrating elliptic cylinders. Part 2. Approximate viscous solution, *J. Fluid Mech.*, *351*, 119–138.

Khatiwala, S. (2003), Generation of internal tides in an ocean of finite depth: Analytical and numerical calculations, *Deep Sea Res., Part I*, *50*, 3–21, doi:10.1016/S0967-0637(02)00132-2.

King, B., H. P. Zhang, and H. L. Swinney (2009), Tidal flow over three-dimensional topography in a stratified fluid, *Phys. Fluids*, *21*(11), 116,601, doi:10.1063/1.3253692.

King, B., H. P. Zhang, and H. L. Swinney (2010), Tidal flow over three-dimensional topography generates out-of-forcing-plane harmonics, *Geophys. Res. Lett.*, *37*, L14606, doi:10.1029/2010GL043221.

King, B., M. Stone, H. P. Zhang, T. Gerkema, M. Marder, R. B. Scott, and H. L. Swinney (2012), Buoyancy frequency profiles and internal semidiurnal tide turning depths in the oceans, *J. Geophys. Res. Oceans*, *117*, C04008, doi:10.1029/2011JC007681.

Kistovich, Y. V., and Y. D. Chashechkin (1998), Linear theory of the propagation of internal wave beams in an arbitrarily stratified liquid, *J. Appl. Mech. Tech. Phys.*, *39*, 729–737.

Klymak, J. M., J. N. Moum, J. D. Nash, E. Kunze, J. B. Girton, G. S. Carter, C. M. Lee, T. B. Sanford, and M. C. Gregg (2006), An estimate of tidal energy lost to turbulence at the Hawaiian Ridge, *J. Phys. Oceanogr.*, *36*, 1148–1164, doi:10.1175/JPO2885.1.

Kunze, E., and J. M. Toole (1997), Tidally driven vorticity, diurnal shear, and turbulence atop Fieberling seamount, *J. Phys. Oceanogr.*, *27*, 2663–2693, doi:10.1175/1520-0485(1997)027¡2663:TDVDSA¿2.0.CO;2.

Llewellyn Smith, S. G., and W. R. Young (2002), Conversion of the barotropic tide, *J. Phys. Oceanogr.*, *32*, 1554–1566, doi:10.1175/1520-0485(2002)032¡1554:COTBT¿2.0.CO;2.

Llewellyn Smith, S. G., and W. R. Young (2003), Tidal conversion at a very steep ridge, *J. Fluid Mech.*, *495*, 175–191, doi:10.1017/S0022112003006098.

Lueck, R. G., and T. D. Mudge (1997), Topographically induced mixing around a shallow seamount, *Science*, *276*(5320), 1831–1833, doi:10.1126/science.276.5320.1831.

Mahesh, K., G. Constantinescu, and P. Moin (2004), A numerical method for large-eddy simulation in complex geometries, *J. Comput. Phys.*, *197*, 215–240, doi:10.1016/j.jcp.2003.11.031.

Melet, A., M. Nikurashin, C. Muller, S. Falahat, J. Nycander, P. G. Timko, B. K. Arbic, and J. A. Goff (2013), Internal tide generation by abyssal hills using analytical theory, *J. Geophys. Res. Oceans*, *118*, 6303–6318, doi:10.1002/2013JC009212.

Moum, J. N., D. R. Caldwell, J. D. Nash, and G. D. Gunderson (2002), Observations of boundary mixing over the continental slope, *J. Phys. Oceanogr.*, *32*, 2113–2130.

Mowbray, D. E., and B. S. H. Rarity (1967), A theoretical and experimental investigation of the phase configuration of internal waves of small amplitude in a density stratified liquid, *J. Fluid Mech.*, *28*, 1–16, doi:10.1017/S0022112067001867.

Munk, W. (1981), Internal waves and small-scale processes, in *Evolution of Physical Oceanography*, chap. 9, edited by B. A. Warren and C. Wunsch, pp. 264–291, MIT Press, Cambridge, Mass.

Munk, W., and C. Wunsch (1998), Abyssal recipes II: Energetics of tidal and wind mixing, *Deep Sea Res., Part I*, *45*, 1977–2010.

Nash, J. D., E. Kunze, J. M. Toole, and R. W. Schmitt (2004), Internal tide reflection and turbulent mixing on the continental slope, *J. Phys. Oceanogr.*, *34*, 1117–1134.

Nycander, J. (2006), Tidal generation of internal waves from a periodic array of steep ridges, *J. Fluid Mech.*, *567*, 415–432, doi:10.1017/S002211200600228X.

Paoletti, M. S., and H. L. Swinney (2012), Propagating and evanescent internal waves in a deep ocean model, *J. Fluid Mech.*, *706*, 571–583, doi:10.1017/jfm.2012.284.

Pétrélis, F., S. G. Llewellyn Smith, and W. R. Young (2006), Tidal conversion at a submarine ridge, *J. Phys. Oceanogr.*, *36*, 1053–1071, doi:10.1175/JPO2879.1.

Polzin, K. L., J. M. Toole, J. R. Ledwell, and R. W. Schmitt (1997), Spatial variability of turbulent mixing in the abyssal ocean, *Science*, *276*(5309), 93–96, doi:10.1126/science.276.5309.93.

Qian, H., P.-T. Shaw, and D. S. Ko (2010), Generation of internal waves by barotropic tidal flow over a steep ridge, *Deep Sea Res., Part I*, *57*, 1521–1531, doi:10.1016/j.dsr.2010.09.001.

Rudnick, D. L., et al. (2003), From tides to mixing along the Hawaiian Ridge, *Science*, *301*, 355–358, doi:10.1126/science.1085837.

St Laurent, L. C., J. M. Toole, and R. W. Schmitt (2001), Buoyancy forcing by turbulence above rough topography in the abyssal Brazil Basin, *J. Phys. Oceanogr.*, *31*, 3476–3495.

St Laurent, L. C., S. Stringer, C. Garrett, and D. Perraultjoncas (2003), The generation of internal tides at abrupt topography, *Deep Sea Res., Part I*, *50*, 987–1003, doi:10.1016/S0967-0637(03)00096-7.

Sutherland, B. (2010), *Internal Gravity Waves*, Cambridge Univ. Press, Cambridge, U. K.

World Ocean Circulation Experiment (1994), *World Ocean Circulation Experiment Southern Ocean Atlas: Program Information*, Dep. of Oceanogr., Texas A&M Univ., College Station. [Available at http://woceatlas.tamu.edu/Sites/html/atlas/SOA_WOCE.html.]

Wunsch, C., and R. Ferrari (2004), Vertical mixing, energy and the general circulation of the oceans, *Annu. Rev. Fluid Mech.*, *36*, 281–314.

Zarroug, M., J. Nycander, and K. Döös (2010), Energetics of tidally generated internal waves for nonuniform stratification, *Tellus, Ser. A*, *62*, 71–79, doi:10.1111/j.1600-0870.2009.00415.x.

Zhang, L., and H. L. Swinney (2014), Virtual seafloor reduces internal wave generation by tidal flow, *Phys. Rev. Lett.*, in press.